European Journal of Medical Research

RESEARCH

Open Access

Prediction models after hepatectomy for hepatocellular carcinoma-based ultrasonic radiomics: an observational study

Dong Jiang[1†], Jialun Ren[1†], Yi Qian[1†], Yijun Gu[1], Ru Wang[1], Hua Yu[2], Hui Dong[2], Dongyu Chen[1], Yan Chen[1], Haozheng Jiang[3] and Yiran Li[1*]

Abstract

Background This study aims to develop and validate predictive models for postoperative complications and early recurrence in hepatocellular carcinoma (HCC) patients.

Methods In a 7:3 ratio, 633 post-hepatectomy HCC patients were modeled and validated. Using 1561 radiomic features from two-dimensional shear wave elastography (2D-SWE), predictive models for the Comprehensive Complication Index (CCI) and recurrence were constructed, refined by LASSO regression, and integrated with clinical and pathologic data. Model performance was assessed using calibration plots and AUCs.

Results The CCI model included Rad signature ($P<0.001$), platelet count ($P=0.012$), neutrophil levels ($P=0.032$), Emax ($P=0.023$), and differentiation status ($P=0.045$), with AUCs of 0.896 for the modeling cohort and 0.832 for validation. The recurrence model included Rad signature ($P<0.001$), arginase ($P=0.038$), patient age ($P=0.001$), adjacent tissue's Emean ($P=0.009$), and blood flow ($P=0.03$), with AUCs of 0.854 and 0.844 for modeling and validation cohorts, respectively. The Rad signature AUC of 0.884 surpassed the nomogram's AUC of 0.854 in the modeling set.

Conclusion Radiomic-based CCI and recurrence models effectively predict complications and short-term recurrence in post-hepatectomy HCC patients, aiding in identifying high-risk individuals for timely intervention.

Keywords Ultrasound radiomics, Hepatocellular carcinoma, Liver resection

The prevalence of hepatocellular carcinoma (HCC) has been on the rise annually, with hepatectomy currently standing as the main therapeutic approach for such malignancy [1, 2]. Following this surgical intervention, the challenges for patients extend beyond typical postoperative complications. They are additionally burdened with the heightened functional demand placed upon the residual liver tissue [3]. Particularly for those already grappling with compromised liver functions, the surgical procedure might precipitate liver inadequacy or decompensation. This could further cascade into grave complications encompassing conditions like ascites, hepatic encephalopathy, and failures of the liver, kidney, and multiple organs [4, 5].

†Dong Jiang, Jialun Ren, and Yi Qian contributed equally to this work.

*Correspondence:
Yiran Li
liyiranehsh@sina.com
[1] Department of Ultrasonography, Shanghai Eastern Hepatobiliary Surgery Hospital, The Third Affiliated Hospital of Naval Medical University, Shanghai 200438, China
[2] Department of Pathology, Shanghai Eastern Hepatobiliary Surgery Hospital, Shanghai 200438, China
[3] Department of Anthropology, College of Arts and Sciences, Case Western Reserve University, Cleveland, OH, USA

© The Author(s) 2025. **Open Access** This article is licensed under a Creative Commons Attribution-NonCommercial-NoDerivatives 4.0 International License, which permits any non-commercial use, sharing, distribution and reproduction in any medium or format, as long as you give appropriate credit to the original author(s) and the source, provide a link to the Creative Commons licence, and indicate if you modified the licensed material. You do not have permission under this licence to share adapted material derived from this article or parts of it. The images or other third party material in this article are included in the article's Creative Commons licence, unless indicated otherwise in a credit line to the material. If material is not included in the article's Creative Commons licence and your intended use is not permitted by statutory regulation or exceeds the permitted use, you will need to obtain permission directly from the copyright holder. To view a copy of this licence, visit http://creativecommons.org/licenses/by-nc-nd/4.0/.

In patients undergoing initial hepatectomy for HCC, the recurrence rates within the first year show variation, and notably, early recurrence is associated with a more unfavorable prognosis than late recurrence [6–8]. Recognizing the significance of this subject is growing, especially given that diverse factors influence the specific rate of recurrence. TACE has been shown to reduce the likelihood of recurrence in certain patient groups [9]. Given these factors, it is imperative to pinpoint patients at heightened risk with precision. Presently, several prognostic models such as MELD (Model for End-Stage Liver Disease) [10], ALBI (Albumin–Bilirubin) [11, 12], and POSSUM (Physiological and Operative Severity Score for the enumeration of Mortality and Morbidity) [13] are in use clinically to forecast severe complications and recurrence post-hepatectomy. Nonetheless, there is an evident gap in tools that synergize imaging metrics with clinical indices. Liver elasticity measurements might hold promise in disease forecasting [14, 15].

The field of radiomics has gained significant traction in the development of clinical prognostic models, showcasing several strengths [16, 17]. Particularly, the convergence of two-dimensional shear wave elastography (2D-SWE) with radiomics encapsulates the synergy of ultrasound elastography and radiomics methodologies. This combination offers a non-invasive approach that provides real-time imaging, precise quantification, and a comprehensive multi-parameter analysis. When these radiomic attributes are coalesced with clinical data, pathologic findings, immunohistochemical details, and other pertinent indicators, there is a notable enhancement in the precision of predictive models.

To improve the predictive accuracy for patients undergoing hepatectomy, the Comprehensive Complication Index (CCI) model and the recurrence model have been formulated. These models incorporate the nuances of 2D-SWE radiomic features alongside other salient features. The potential enhancements within the realm of 2D-SWE radiomics in these specific domains are anticipated. The community looks forward to the subsequent external validation of these models.

Materials and methods

Population enrollment

The research undertaken at the Eastern Hepatobiliary Surgery Hospital in China followed a prospective, single-center study design. Ethical clearance was granted by the institution's ethics committees under the approval number EHBHKY2021-K-011. Prior to their inclusion, every individual provided informed consent. From September 2021 to September 2023, 800 patients diagnosed with HCC––confirmed pathologically after surgery. However, specific criteria led to the exclusion of some patients, including those aged below 18 or above 75, those identified with distant metastasis through Contrast-enhanced computed tomography (CT) or magnetic resonance imaging (MRI), individuals who underwent preoperative interventions like radiation or chemotherapy, and those who received postoperative procedures like TACE. Following these criteria, 633 patients were deemed eligible for the study. These participants were then categorized into two groups, the modeling group and the validation group, in a 7:3 ratio, according to varied predictive outcomes (See Fig. 1).

The routine data acquisition for patients encompasses several key elements: (1) demographic details and clinical descriptors, capturing attributes like age, gender, existing health conditions, and any history of antiviral therapies; (2) results from various laboratory tests, notably full blood analysis, assessments of liver functionality, and coagulation metrics; (3) ultrasound-derived parameters such as count, dominant diameter, blood flow dynamics, echo characteristics, and rigidity evaluations; (4) determinants from pathological and immunohistochemical assessments that include differentiation levels, the presence of markers like arginase, GPC-3, and Hep-1; and (5) a meticulous record of the therapeutic interventions administered and subsequent monitoring sessions.

CCI and details of treatment

In this research, the CCI serves as a tool for evaluating postoperative complications [18]. Designed to gauge the collective impact of these complications on surgical patients, the CCI integrates both the severity and cumulative consequences on patient prognosis [19]. This index operates through a bifurcated approach. Initially, it pinpoints and records all complications emerging within a defined period, often within the initial 30 days post-surgery. Subsequently, each of these complications receives a grade based on the Clavien–Dindo classification metrics

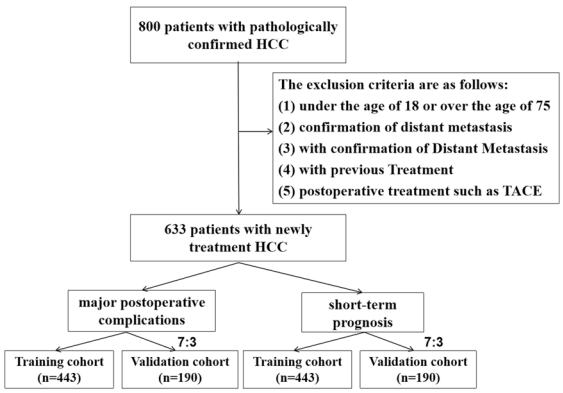

Fig. 1 Flowchart showing the enrollment of patients

[21]. The CCI is derived by aggregating the values associated with every registered complication. When the CCI score surpasses a threshold, such as 26.2, it signifies a pronounced severity and comprehensive influence of the postoperative complications.

Prior to embarking on hepatectomy procedures, a comprehensive assessment of hepatic function is mandatorily conducted by the designated surgeon. During the operation, meticulous attention ensures margins devoid of malignant remnants. The duration for hepatic inflow occlusion remains strictly capped at 20 min. Following the surgery, vigilant postoperative care is imperative, encompassing appropriate pain management, fluid balance regulation, and the deployment of prophylactic antibiotics.

2D-SWE evaluation

Utilizing the Acuson Sequoia diagnostic ultrasound apparatus (Siemens Healthineers, Mountain View, California, USA) paired with a 5C1 convex abdominal transducer, conventional ultrasound diagnostics were performed. Prior to the procedure, patients underwent a fasting period spanning a minimum of 8 h. Liver ultrasonography targeting solid liver anomalies was conducted by a seasoned sonographer boasting over a decade and a half in expertise. Subsequent to this standard ultrasound protocol, another specialist adept in ultrasound elastography executed 2D-SWE evaluations using the aforementioned apparatus and transducer. The procedure was carried out devoid of external pressure. With the activation of the 2D-SWE mode, visual representation of the targeted hepatic carcinoma anomaly emerged on the device screens. A delineated region of interest (ROI) was established, encapsulating both the anomaly and proximate hepatic tissue. A green representation of the lesion in the quality imagery signified attainment of the set quality threshold for the 2D-SWE illustration. Shear wave velocity measurements ranged from 0.5 to 4.0 m/s. Circular ROIs were positioned both at the densest segment of the tumor and its outer boundary. Peak ROI measurements were termed Emax, while the mean was designated Emean [22]. For every anomaly, each lesion was evaluated three times [23]. Refer to Fig. 2 for a visual illustration.

Segmentation of ROIs and radiomic feature extraction

When discrepancies in observations arose from the interpretation of identical images, including those of target anomalies, a trio of sonographers deliberated to attain a unanimous decision before embarking on ROI delineation. Using the freely available 3D Slicer software V4.10.2 (https://www.slicer.org/), a pair of sonographers delineated the ROIs for each target anomaly, as illustrated in Fig. 3. To ensure consistency and objectivity, two experienced investigators (Radiologist A with 8 years of abdominal ultrasound experience and Radiologist B with 5 years of experience in hepatic imaging) were responsible for ROI segmentation and radiomic feature extraction. Both investigators were blinded to clinical outcomes and histopathological results during the segmentation process. To assess the reproducibility of radiomic feature extraction, inter-observer agreement was evaluated. A random subset of 30 cases was independently segmented by both investigators, and the extracted features were compared using the ICC. Features with ICC > 0.80 were considered to have good reliability and were retained for further analysis. The manually derived features encompass three distinct categories: (I) geometric attributes, (II) intensity parameters, and (III) texture descriptors. While geometric attributes elucidate the tumor's three-dimensional structural nuances, intensity parameters convey the primary statistical distribution associated with voxel intensities located within the tumor. Conversely, texture descriptors illuminate patterns or spatial configurations of secondary and more advanced intensity orders. Such texture descriptors undergo extraction through a variety of techniques, encompassing gray level co-occurrence matrix (GLCM), gray level run length matrix (GLRLM), gray level size zone matrix (GLSZM), and neighborhood gray tone difference matrix (NGTDM) methodologies. For the purposes of this study, the tumor's ROI encompassed its entire volumetric representation, evident in Fig. 3. Leveraging the 3D Slicer software, equipped with the advanced PyRadiomics package plugin (https://www.radiomics.io/pyradiomics.html), a total of 1561 radiomic features underwent extraction for each delineated ROI.

Feature selection and Rad signature

A statistical assessment using the Mann–Whitney U test was undertaken for all radiomic attributes. Radiomic characteristics with a significance level (P value) less than 0.05 were maintained for further analysis. When evaluating features known for their high reproducibility, the correlation among these features was determined using Spearman's rank correlation coefficient. From any pair of features with a correlation coefficient exceeding 0.9, only one was selected for retention. To ensure the most comprehensive representation of features, a methodical approach of greedy recursive elimination was employed. Specifically, during each iteration, the most redundant attribute from the current set was removed.

To construct the signature, the Least Absolute Shrinkage and Selection Operator (LASSO) regression technique was applied to the detection dataset. LASSO aims to drive the regression coefficients toward zero based on the regulatory weight, which effectively zeroes

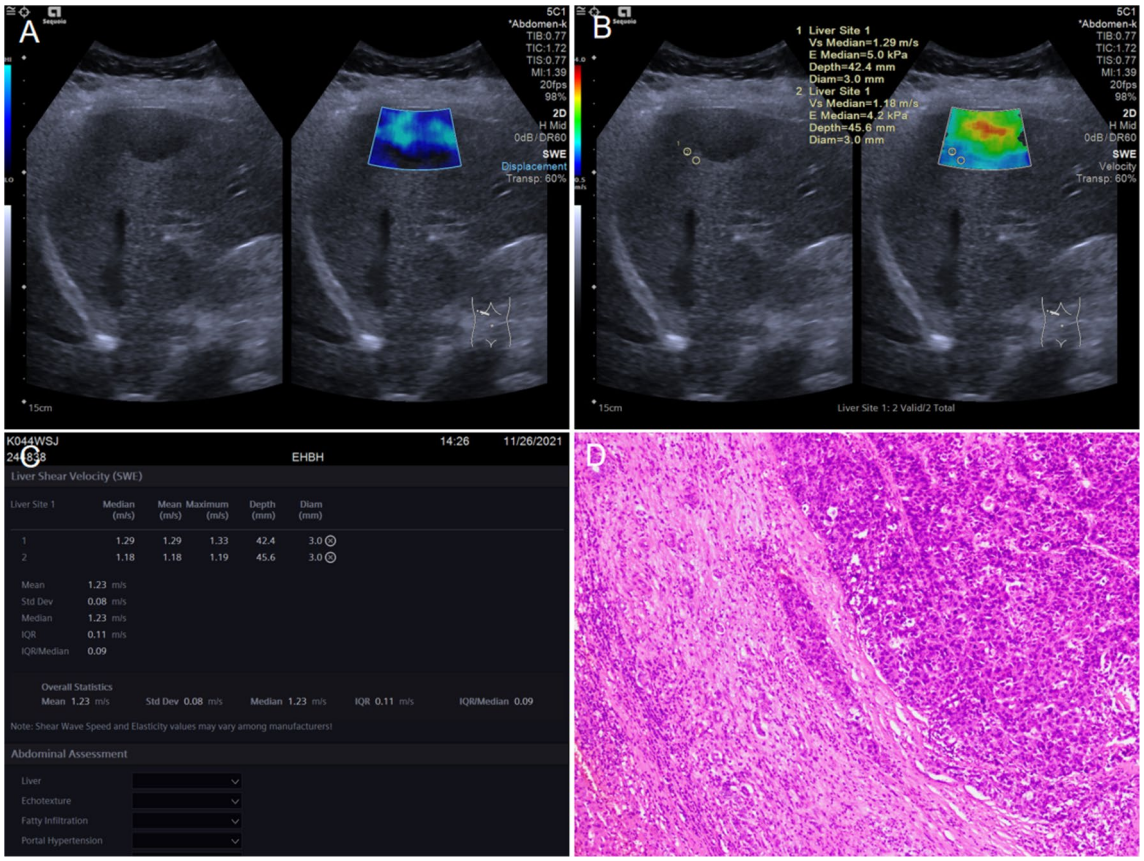

Fig. 2 2D-SWE used to assess localized liver lesions in this study: **A**. Tumors displayed in the green mass mode, indicating that 2D-SWE's accuracy meets the standard. For tumors displayed in speed mode, its velocity scale was configured within the range of 0.5 to 4.0 m per second; **B**. Two round areas of interest (ROIs) placed at the hardest part of the tumor and around the tumor, each with a diameter of 3 mm; **C**. The maximum and mean elasticity of these ROIs, denoted as Emax and Emean,; **D**. surgical pathology of HCC(HE × 100)

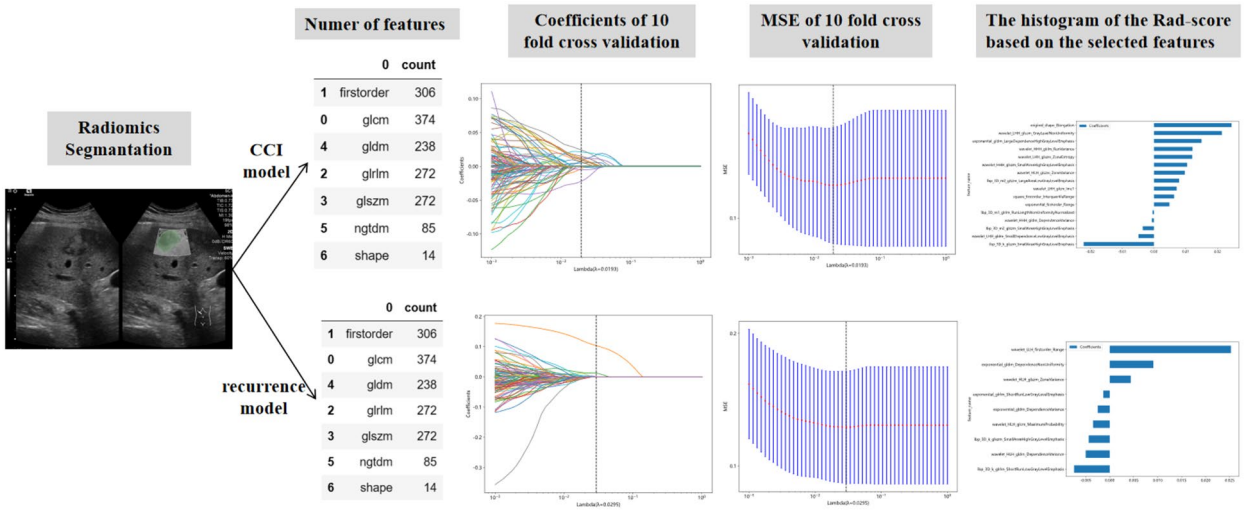

Fig. 3 Features statistics and LASSO feature selection

out coefficients of less relevant attributes. The strategy involved using tenfold cross-validation, targeting the minimum criteria for determining an optimal regularization parameter, and this was pinpointed by noting the least cross-validation error. Subsequently, the attributes with coefficients that did not equate to zero were incorporated into the regression analysis and amalgamated to formulate a radiomics signature. A radiomics score was derived for every patient using a linear combination of the preserved attributes, adjusted using their respective coefficients from the model. For executing the LASSO regression, the scikit-learn library in Python was utilized. Following this approach, a subset of functions was preserved for further consideration (Fig. 3).

Following the feature selection process via LASSO, the refined features were incorporated into machine learning algorithms, notably SVM, LR, MLP, KNN, and XGBoost, to establish a risk model. Utilizing a five-fold cross-validation technique, a conclusive wheel signature was derived (Fig. 3). For a comprehensive and effective appraisal of the added prognostic significance that the radiomics signature provided when juxtaposed with clinical risk factors, a radiomics nomogram was devised specifically for the validation dataset. This nomogram synthesized the insights from the radiomics signature and the clinical risk indicators as interpreted through SVM. To gauge the congruence between the nomogram's predicted outcomes post-hepatectomy and the genuine observed results, a calibration curve was formulated. The calibration capabilities of the nomogram were assessed using the Hosmer–Lemeshow test. Additionally, the decision curve analysis (DCA) was employed to determine the potential clinical benefit of the model.

Data splitting and preprocessing strategy to prevent data Leakage

To prevent potential data leakage and ensure the methodological rigor of the analysis, the dataset was first randomly divided into a training (modeling) cohort and a validation cohort in a 7:3 ratio before any data preprocessing was performed. All subsequent preprocessing steps—including outlier detection, missing data imputation, and z-score standardization—were conducted exclusively within the training cohort. The imputation values and standardization parameters derived from the training set were subsequently applied to the validation cohort to maintain strict separation between the two datasets. Feature selection, including LASSO regression, as well as model construction, was also carried out solely within the training cohort. The final model's predictive performance was evaluated using the independent validation cohort. This pipeline was specifically designed to avoid information leakage from the validation set into the model training process and to ensure a robust and generalizable evaluation of model performance.

Follow-up

Every patient underwent consistent monitoring in the outpatient setting. Routine procedures entailed conducting physical evaluations and laboratory assays, of which alpha-fetoprotein (AFP) quantification and ultrasound evaluations stood out, occurring with a frequency spanning 3–6 months. Imaging studies, such as CT and MRI, were customarily scheduled semiannually. Tumor recurrence was defined as the appearance of new intrahepatic or extrahepatic lesions with arterial phase enhancement and portal venous washout, either at or near the primary tumor site. In cases where recurrence was suspected, treatment strategies such as TACE or radiofrequency/microwave ablation were selected based on tumor characteristics and patient condition. The criteria for recurrence encompassed the emergence of novel lesions proximal to the initial site or anywhere within hepatic or extrahepatic locations, which demonstrated arterial intensification and portal venous phase contrast clearance. Moreover, to address missing or incomplete follow-up data, patients lost to follow-up were censored at the time of their last documented visit. Data completeness was ensured by cross-checking hospital electronic medical records and, when necessary, contacting patients or their families by phone to verify outcomes. The statistical inferences were grounded on datasets accrued prior to September 1, 2023.

Statistical methods

For the data analytics, both IBM's SPSS Statistics 28 and the R software suite (version 4.0.3, sourced from the R Foundation for Statistical Computing in Vienna, Austria) were utilized. Continuous variables are expressed as mean ± standard deviation (SD) if they followed a normal distribution, and were compared using the independent samples t-test. For non-normally distributed data, the Mann–Whitney U test was applied. Categorical variables are summarized as counts and percentages, and were analyzed using either the chi-square test or Fisher's exact test, depending on sample size and expected frequencies. Variables were stratified according to clinical outcomes to facilitate comparative analyses. To identify potential predictive factors, univariate analyses were first conducted. Variables with a P value < 0.05 were subsequently included in a multivariate stepwise logistic regression model to estimate odds ratios (ORs) and corresponding 95% confidence intervals (CIs). In addition, variables with an area under the receiver operating characteristic curve (AUC) greater than 0.7 were considered to have good predictive performance and included in

the final nomogram. The predictive performance of the nomogram was evaluated using the concordance index (C-index), and its generalizability was assessed by validating the model in an independent validation cohort using R software. Furthermore, to explore machine learning-based risk modeling, support vector machine (SVM) and other algorithms were employed using selected features. The performance of each model was assessed using AUC and calibration metrics.

Results

Clinical characteristics of patients

An examination of clinical features was undertaken, spanning demographics, clinical data, laboratory findings, ultrasonic determinants, and the information derived from pathology and immunohistochemistry. To serve as focal points for this study, predictive frameworks were fashioned for both CCI and potential recurrence. Tables 1 and 2 portray a comparative overview of these clinical features within the training and validation cohorts. Notably, aspects such as age, BMI, and nationality displayed no significant variance between the two sets of patients, as evidenced by a P value exceeding 0.05. Thus, only those markers showing notable disparities underwent subsequent scrutiny.

Features statistics and LASSO feature selection

A total of 1561 hand-engineered features have been isolated for examination. This comprises 306 primary features, 14 delineating structural attributes, and the remaining identified as texture related. The extraction process for these hand-engineered attributes was facilitated through a specialized feature study tool, developed internally and anchored on Pyradiomics (refer to http://pyradiomics.readthedocs.io). All related feature statistics, inclusive of the P values, can be referenced in Table 3. To enhance the interpretability of the selected radiomic features, we visualized the top-ranked features from both the CCI and recurrence models based on their LASSO coefficients. Among the 16 selected features in the CCI model, exponential_firstorder_Range represents the intensity spread in the exponential-transformed ultrasound image. This feature may reflect intra-tumoral heterogeneity related to necrosis, hemorrhage, or fibrosis, all of which are commonly observed in HCC and are known to increase the risk of postoperative complications. The lbp_3D_k_glszm_SmallAreaHighGrayLevelEmphasis feature indicates the presence of small, bright texture zones, which may correlate with microvascular invasion or necrosis patterns. In the recurrence model, features like exponential_glrlm_ShortRunLowGrayLevelEmphasis quantify the frequency of short homogeneous runs with low intensity, possibly reflecting irregular tumor margins or poor differentiation. These imaging-derived microstructural cues may reflect subtle biological processes such as angiogenesis, stromal remodeling, or satellite nodule formation that are difficult to assess visually but are captured quantitatively through radiomic analysis. Examining the Spearman correlation coefficients reveals the intrinsic relationships across clinical attributes. It becomes evident that parameters such as the long diameter, short diameter, and a general diameter exhibit the strongest correlation ties. Features with non-null coefficients were shortlisted for wheel score calculation, executed through the LASSO logistic regression methodology. The outcome of this, including coefficients and MSE from a tenfold validation process, is presented subsequently. A visual representation, Fig. 3, depicts the wheel score, while a histogram, grounded on the chosen attributes, displays the coefficient values for the finalized non-null features.

Univariate and multivariate analyses of clinical characteristics

Within the cohort training the CCI model, notable associations emerged upon multivariate scrutiny. Specifically, associations with platelets ($P=0.012$), neutrophils ($P=0.032$), differentiation attributes ($P=0.045$), and Emax ($P=0.023$) were evident as depicted in Table S1. Similarly, when examining the training cohort for the recurrence model, distinct associations with factors like age ($P=0.001$), arginase levels ($P=0.038$), circulatory blood flow ($P=0.03$), and the mean of paracancerous readings ($P=0.009$) were brought to light in Table S2. The efficacy of the ultrasound signature was evaluated using several advanced machine learning algorithms. Among these, the SVM model emerged superior. In comparing this signature's efficacy against classifiers like KNN, ExtraTrees, XGBoost, and LightGBM, the optimal model was identified, with results given in Tables S3 and S4. Consequently, for the formulation of the clinical signature, the SVM was the chosen foundational model. Performance metrics indicated that for the CCI model, the SVM technique registered an AUC of 0.724 (95% CI 0.6538–0.7933) within the training dataset and an AUC of 0.647 (95% CI 0.5799–0.7142) in its validation counterpart. Meanwhile, in the replication framework, SVM's efficacy was marked by an AUC of 0.574 (95% CI 0.5012–0.6468) for the training set and an AUC of 0.552 (95% CI 0.4826–0.6209) for the validation dataset.

Performance of the radiomics models

Within the training set, both the clinical and wheel signatures achieved a good model fit, as depicted in Table 4. Moving to the validation set, an overly precise fit was evident for the clinical signature, while the

Table 1 Baseline characteristics of patients in two cohorts

characters	ALL ($n=633$)	Training cohort ($n=443$)			Validation cohort ($n=190$)		
		CCI < 26.2 ($n=380$)	CCI ≥ 26.2 ($n=63$)	*P* value	CCI < 26.2 ($n=162$)	CCI ≥ 26.2 ($n=28$)	*P* value
Age (y)	56.02 ± 10.63	55.36 ± 10.72	57.68 ± 10.17	0.068	56.57 ± 10.99	57.96 ± 7.51	0.947
BMI(kg/m^2)	24.03 ± 3.22	24.17 ± 3.32	23.86 ± 3.27	0.472	23.73 ± 3.01	24.23 ± 2.88	0.339
Gender							
M	488(77.09)	282(74.21)	58(92.06)	0.003	120(74.1)	28(100.00)	0.005
F	145(22.91)	98(25.79)	5(7.94)		42(25.9)	0(0)	
Nation							
Han	615(97.16)	370(97.37)	63(100.00)	0.398	154(95.06)	28(100.00)	0.489
Ethnic	18(2.84)	10(2.63)	0(0)		8(4.94)	0(0)	
COPD							
N	603(93.3)	361(95)	61(96.9)	0.511	155(95.7)	26(92.6)	0.481
Y	30(4.7)	19(5)	2(3.1)		7(4.3)	2(7.4)	
T2DM							
N	570(90)	341(89.7)	57(90.6)	0.823	146(90.2)	26(92.6)	0.692
Y	63(10)	39(10.3)	6(9.4)		16(9.8)	2(7.4)	
Hypertension							
N	583(92.1)	350(92.1)	58(92.2)	0.977	148(91.4)	27(96.3)	0.383
Y	50(7.9)	30(7.9)	5(7.8)		14(8.6)	1(3.7)	
Tumor history							
N	599(94.63)	361(95.00)	60(95.24)	1.0	152(93.83)	26(92.86)	1.0
Y	34(5.37)	19(5.00)	3(4.76)		10(6.17)	2(7.14)	
Hepatitis							
N	276(43.60)	168(44.21)	22(34.92)	0.214	78(48.15)	8(28.57)	0.086
Y	357(56.40)	212(55.79)	41(65.08)		84(51.85)	20(71.43)	
Antiviral_drug							
N	430(67.93)	250(65.79)	39(61.90)	0.648	119(73.46)	22(78.57)	0.736
Y	203(32.07)	130(34.21)	24(38.10)		43(26.54)	6(21.43)	
Number							
Single	505(79.78)	307(80.79)	51(80.95)	1.0	125(77.16)	22(78.57)	1.0
Multiple	128(20.22)	73(19.21)	12(19.05)		37(22.84)	6(21.43)	
Resection							
< 3 segments	603(95.26)	361(95.00)	60(95.24)	1.0	155(95.68)	27(96.43)	1.0
≥ 3 segments	30(4.74)	19(5.00)	3(4.76)		7(4.32)	1(3.57)	
Cirrhosis							
N	235(37.12)	137(36.05)	21(33.33)	0.783	65(40.12)	12(42.86)	0.949
Y	398(62.88)	243(63.95)	42(66.67)		97(59.88)	16(57.14)	
Total albumin	67.62 ± 5.43	67.72 ± 5.46	67.93 ± 5.47	0.99	67.33 ± 5.44	67.17 ± 5.13	0.684
Albumin	41.34 ± 3.98	41.25 ± 4.00	41.95 ± 4.35	0.122	41.24 ± 3.79	41.76 ± 4.12	0.316
ALT	37.17 ± 45.67	36.97 ± 45.96	36.32 ± 42.40	0.672	36.53 ± 38.50	45.43 ± 78.18	0.642
AST	33.69 ± 31.29	33.77 ± 33.01	29.94 ± 14.98	0.902	35.46 ± 33.51	30.86 ± 18.95	0.598
GGT	74.31 ± 76.88	74.03 ± 78.23	82.49 ± 79.76	0.128	71.90 ± 76.38	73.68 ± 53.44	0.158
INR	1.00 ± 0.10	1.00 ± 0.09	1.01 ± 0.11	0.601	1.00 ± 0.09	1.01 ± 0.10	0.804
PT	12.02 ± 1.13	12.00 ± 1.17	12.15 ± 1.16	0.58	11.98 ± 1.03	12.13 ± 1.12	0.763
PLT	172.55 ± 69.40	175.16 ± 70.48	153.68 ± 51.07	0.017	176.87 ± 72.23	154.61 ± 67.34	0.101
N	3.56 ± 1.29	3.50 ± 1.16	3.92 ± 1.93	0.408	3.52 ± 1.26	3.87 ± 1.18	0.111
Glucose		5.16 ± 0.79	5.22 ± 1.19	0.134	5.18 ± 0.81	5.04 ± 0.74	0.169
Tumor size(mm)	51.26 ± 29.43	50.09 ± 29.41	58.04 ± 32.83	0.044	51.22 ± 27.61	52.24 ± 31.55	0.996
MVI							
N	345(54.5)	214(56.3)	24(38.1)	0.030	97(59.9)	10(35.7)	0.013

Table 1 (continued)

characters	ALL ($n=633$)	Training cohort ($n=443$)			Validation cohort ($n=190$)		
		CCI < 26.2 ($n=380$)	CCI ≥ 26.2 ($n=63$)	*P* value	CCI < 26.2 ($n=162$)	CCI ≥ 26.2 ($n=28$)	*P* value
Y	288(45.5)	166(43.7)	39(61.9)		65(40.1)	18(64.3)	
Hep-1							
N	325(51.3)	210(55.3)	19(30.2)	0.001	88(54.3)	8(28.6)	0.045
Y	308(48.7)	170(44.7)	44(69.8)		74(45.7)	20(71.4)	
Arginase							
N	296(46.8)	196(51.6)	12(18)	< 0.001	81(50)	7(25)	0.014
Y	337(53.2)	184(48.4)	51(81)		81(50)	21(75)	
GPC-3							
N	333(52.6)	215(56.6)	21(33.3)	< 0.001	90(55.6)	7(25)	0.010
Y	300(47.4)	165(43.4)	42(66.7)		72(44.4)	21(75)	
CD34							
N	249(39.3)	167(43.9)	9(14.3)	< 0.001	68(42)	5(17.9)	0.053
Y	384(60.7)	213(56.1)	54(85.7)		94(58)	23(82.1)	
Histology							
Massive or Nodular	328(51.82)	181(47.63)	47(74.60)	< 0.001	82(50.62)	18(64.29)	0.005
Tubular or Solid	113(17.85)	70(18.42)	13(20.63)		22(13.58)	8(28.57)	
Others	192(30.33)	129(33.95)	3(4.76)		58(35.80)	2(7.14)	
Differentiated							
Medium or high	293(46.29)	193(50.79)	15(23.81)	< 0.001	77(47.53)	8(28.57)	0.097
Low	340(53.71)	187(49.21)	48(76.19)		85(52.47)	20(71.43)	
Shape							
Circular	332(52.45)	200(52.63)	36(57.14)	0.597	81(50.00)	15(53.57)	0.885
Ellipse	301(47.55)	180(47.37)	27(42.86)		81(50.00)	13(46.43)	
Echo							
Low	445(70.30)	274(72.11)	42(66.67)	0.463	112(69.14)	17(60.71)	0.508
High	188(29.70)	106(27.89)	21(33.33)		50(30.86)	11(39.29)	
Edge							
Smooth	342(54.03)	205(53.95)	31(49.21)	0.574	88(54.32)	18(64.29)	0.439
Rough	291(45.97)	175(46.05)	32(50.79)		74(45.68)	10(35.71)	
Blood flow							
N	216(34.12)	132(34.74)	20(31.75)	0.749	58(35.80)	6(21.43)	0.204
Y	417(65.88)	248(65.26)	43(68.25)		104(64.20)	22(78.57)	
Paracancerous Emax	1.64 ± 1.30	1.69 ± 1.64	1.62 ± 0.39	0.119	1.51 ± 0.42	1.61 ± 0.33	0.122
Paracancerous Emean	1.46 ± 0.39	1.45 ± 0.39	1.52 ± 0.42	0.136	1.44 ± 0.41	1.52 ± 0.31	0.125
Emax	2.41 ± 1.06	2.37 ± 0.88	2.86 ± 2.24	0.008	2.35 ± 0.73	2.19 ± 0.53	0.264
Emean	1.84 ± 0.49	1.82 ± 0.46	1.98 ± 0.59	0.046	1.84 ± 0.52	1.71 ± 0.43	0.073

M man, *F* female, *N* no, *Y* yes, *HDL* High-density lipoprotein, *LDL* Low-density lipoprotein, *ALT* alanine aminotransferase, *AST* aspartate aminotransferase, *GGT* γ-glutamyl transpeptidase, *N* neutrophil, *PT* prothrombin time, *INR* International normalized ratio, *Tumor size* maximum dimension of the tumor, *MVI* microvascular invasion, *Emax* Max values of tumor, *Emean* average values of tumor, *Paracancerous Emax* Max values of tumor periphery, *Paracancerous Emean* Average values of tumor, *P* value for comparisons between CCI < 26.2 and CCI ≥ 26.2 patients

radical signature retained a robust fit. An analysis of AUC values across the two models for the wheel signature, within both training and validation cohorts, is visualized in Fig. 4. A composite nomogram for the CCI model was developed integrating both the clinical and wheel signatures, with Fig. 5B highlighting its superior performance. Similarly, an advanced nomogram for the recurrence model, designed with a prior integration of the clinical and wheel signatures, also displayed favorable performance in Fig. 6B. The Delong test, applied to compare the clinical and wheel signatures, including the nomogram, is detailed in Table 5. Nomogram calibration curves, spanning both the training and validation cohorts across two models,

Table 2 Baseline characteristics of patients in two cohorts

Characters	ALL (*n* = 633)	Training cohort (*n* = 443)			Validation cohort (*n* = 190)		
		Not-recurrence (*n* = 380)	Recurrence (*n* = 63)	*P* value	Not-recurrence (*n* = 162)	Recurrence (*n* = 28)	*P* value
Age (y)	56.02 ± 10.63	56.39 ± 10.51	51.96 ± 10.76	0.002	56.63 ± 10.54	57.43 ± 10.68	0.66
BMI(kg/m^2)	24.03 ± 3.22	24.06 ± 3.26	24.50 ± 3.57	0.137	23.92 ± 3.06	23.27 ± 2.60	0.246
Gender							
M	488(77.09)	285(76.41)	55(78.57)	0.811	117(75.48)	31(88.57)	0.144
F	145(22.91)	88(23.59)	15(21.43)		38(24.52)	4(11.43)	
Nation							
Han	615(97.16)	365(97.86)	68(97.14)	1.0	148(95.48)	34(97.14)	1.0
Ethnic	18(2.84)	8(2.14)	2(2.86)		7(4.52)	1(2.86)	
COPD							
N	603(93.3)	364(95.8)	58(92.1)	0.389	154(95.1)	27(96.4)	0.693
Y	30(4.7)	16(4.2)	5(7.9)		8(4.9)	1(3.6)	
T2DM							
N	570(90)	342(90)	56(88.9)	0.795	148(91.3)	24(85.7)	0.431
Y	63(10)	38(10)	7(11.1)		14(8.8)	4(14.3)	
Hypertension							
N	583(92.1)	352(92.6)	56(90.7)	0.614	148(91.4)	27(96.4)	0.313
Y	50(7.9)	28(7.4)	7(9.3)		14(8.6)	1(3.6)	
Tumor history							
N	599(94.63)	354(94.91)	67(95.71)	1.0	144(92.90)	34(97.14)	0.585
Y	34(5.37)	19(5.09)	3(4.29)		11(7.10)	1(2.86)	
Hepatitis							
N	276(43.60)	163(43.70)	27(38.57)	0.507	73(47.10)	13(37.14)	0.379
Y	357(56.40)	210(56.30)	43(61.43)		82(52.90)	22(62.86)	
Antiviral_drug							
N	430(67.93)	241(64.61)	48(68.57)	0.616	118(76.13)	23(65.71)	0.29
Y	203(32.07)	132(35.39)	22(31.43)		37(23.87)	12(34.29)	
Number							
Single	505(79.78)	304(81.50)	54(77.14)	0.494	120(77.42)	27(77.14)	1.0
Multiple	128(20.22)	69(18.50)	16(22.86)		35(22.58)	8(22.86)	
Resection							
< 3 segments	603(95.26)	356(95.44)	65(92.86)	0.539	147(94.84)	35(100.00)	0.364
≥ 3 segments	30(4.74)	17(4.56)	5(7.14)		8(5.16)	null	
Cirrhosis							
N	235(37.12)	130(34.85)	28(40.00)	0.491	61(39.35)	16(45.71)	0.616
Y	398(62.88)	243(65.15)	42(60.00)		94(60.65)	19(54.29)	
Total albumin	67.62 ± 5.43	67.79 ± 5.54	67.53 ± 4.99	0.695	67.31 ± 5.36	67.29 ± 5.57	0.997
Albumin	41.34 ± 3.98	41.32 ± 4.07	41.49 ± 4.00	0.917	41.31 ± 4.03	41.34 ± 2.86	0.854
ALT	37.17 ± 45.67	37.55 ± 48.57	33.29 ± 22.03	0.428	39.40 ± 49.58	30.94 ± 27.13	0.24
AST	33.69 ± 31.29	32.78 ± 32.33	35.56 ± 23.59	0.102	35.28 ± 33.15	32.60 ± 25.16	0.693
GGT	74.31 ± 76.88	73.76 ± 80.87	83.10 ± 63.70	0.021	70.31 ± 66.84	80.37 ± 97.87	0.929
INR	1.00 ± 0.10	1.00 ± 0.09	1.01 ± 0.11	0.78	1.00 ± 0.10	0.99 ± 0.07	0.548
PT	12.02 ± 1.13	11.99 ± 1.16	12.16 ± 1.20	0.721	12.03 ± 1.10	11.89 ± 0.78	0.553
PLT	172.55 ± 69.40	169.88 ± 68.28	183.99 ± 68.47	0.064	170.36 ± 68.19	187.86 ± 85.65	0.448
N	3.56 ± 1.29	3.58 ± 1.31	3.46 ± 1.28	0.305	3.52 ± 1.18	3.77 ± 1.52	0.848
Glucose	5.16 ± 0.84	5.16 ± 0.84	5.20 ± 0.92	0.759	5.17 ± 0.79	5.07 ± 0.85	0.282
Tumor size(mm)	51.26 ± 29.43	49.15 ± 29.76	62.22 ± 29.08	< 0.001	50.59 ± 28.88	54.84 ± 24.66	0.206

Table 2 (continued)

Characters	ALL (*n* = 633)	Training cohort (*n* = 443)			Validation cohort (*n* = 190)		
		Not-recurrence (*n* = 380)	Recurrence (*n* = 63)	*P* value	Not-recurrence (*n* = 162)	Recurrence (*n* = 28)	*P* value
MVI							
N	345(54.5)	214(56.3)	24(38.1)	0.046	97(59.9)	10(35.7)	0.600
Y	288(45.5)	166(43.7)	39(61.9)		65(40.1)	18(64.3)	
Hep-1							
N	325(51.3)	202(53.2)	27(42.9)	0.971	85(52.5)	11(39.2)	0.074
Y	308(48.7)	178(46.8)	36(57.1)		77(47.5)	17(60.7)	
Arginase							
N	296(46.8)	184(48.4)	24(38.1)	0.936	81(50)	7(25)	0.048
Y	337(53.2)	196(51.6)	39(61.9)		81(50)	21(75)	
GPC-3							
N	333(52.6)	206(54.2)	30(47.6)	0.843	92(56.8)	5(17.9)	0.09
Y	300(47.4)	174(45.8)	33(52.4)		70(43.2)	23(82.1)	
CD34							
N	249(39.3)	156(41.1)	20(31.7)	0.815	69(42.6)	4(14.3)	0.123
Y	384(60.7)	224(58.9)	43(68.3)		93(57.4)	24(85.7)	
Histology							
Massive or Nodular	328(51.82)	185(49.60)	43(61.43)	0.019	77(49.68)	23(65.71)	0.194
Tubular or Solid	113(17.85)	67(17.96)	16(22.86)		25(16.13)	5(14.29)	
Others	192(30.33)	121(32.44)	11(15.71)		53(34.19)	7(20.00)	
Differentiated							
Medium or high	293(46.29)	182(48.79)	26(37.14)	0.097	72(46.45)	13(37.14)	0.417
Low	340(53.71)	191(51.21)	44(62.86)		83(53.55)	22(62.86)	
Shape							
Circular	332(52.45)	209(56.03)	27(38.57)	0.011	83(53.55)	13(37.14)	0.117
Ellipse	301(47.55)	164(43.97)	43(61.43)		72(46.45)	22(62.86)	
Echo							
Low	445(70.30)	265(71.05)	51(72.86)	0.87	103(66.45)	26(74.29)	0.486
High	188(29.70)	108(28.95)	19(27.14)		52(33.55)	9(25.71)	
Edge							
Smooth	342(54.03)	204(54.69)	32(45.71)	0.211	89(57.42)	17(48.57)	0.445
Rough	291(45.97)	169(45.31)	38(54.29)		66(42.58)	18(51.43)	
Blood flow							
N	216(34.12)	141(37.80)	11(15.71)	< 0.001	55(35.48)	9(25.71)	0.365
Y	417(65.88)	232(62.20)	59(84.29)		100(64.52)	26(74.29)	
Paracancerous Emax	1.64 ± 1.30	1.68 ± 1.66	1.67 ± 0.40	0.01	1.52 ± 0.43	1.58 ± 0.33	0.134
Paracancerous Emean	1.46 ± 0.39	1.44 ± 0.39	1.58 ± 0.40	0.012	1.45 ± 0.41	1.49 ± 0.32	0.278
Emax	2.41 ± 1.06	2.38 ± 0.88	2.77 ± 2.14	0.015	2.28 ± 0.68	2.54 ± 0.77	0.049
Emean	1.84 ± 0.49	1.82 ± 0.48	1.98 ± 0.47	0.011	1.79 ± 0.50	1.96 ± 0.52	0.047

M man, *F* female, *N* no, *Y* yes, *HDL* High-density lipoprotein, *LDL* Low-density lipoprotein, *ALT* alanine aminotransferase, *AST* aspartate aminotransferase, *GGT* γ-glutamyl transpeptidase, *N* neutrophil, *PT* prothrombin time, *INR* International normalized ratio, *Tumor size* maximum dimension of the tumor, *MVI* microvascular invasion, *Emax* Max values of tumor, *Emean* average values of tumor, *Paracancerous Emax* Max values of tumor periphery, *Paracancerous Emean* Average values of tumor, *P* value for comparisons between not-recurrence and recurrence patients

demonstrate solid agreement (Figs. 5D, 6D). Table S5 showcases the P values from the Hosmer–Lemeshow test, reviewing the clinical, wheel signatures, and nomogram, suggesting the seamless fit of the two model's nomograms across training and validation groups. Remarkably, in predicting recurrence, radiomics, when

Table 3 The results of 2D-SWE radiomics feature selection based on cross-validation

Sequence	Feature number	Individual features
CCI model	16	exponential_firstorder_Range exponential_gldm_LargeDependenceHighGrayLevelEmphasis lbp_3D_k_glszm_SmallAreaHighGrayLevelEmphasis lbp_3D_m1_glrlm_RunLengthNonUniformityNormalized lbp_3D_m2_glszm_LargeAreaLowGrayLevelEmphasis lbp_3D_m2_glszm_SmallAreaHighGrayLevelEmphasis original_shape_Elongation square_firstorder_InterquartileRange wavelet_HHH_gldm_DependenceVariance wavelet_HHH_glrlm_RunVariance wavelet_HHH_glszm_SmallAreaHighGrayLevelEmphasis wavelet_HLH_glszm_ZoneVariance wavelet_LHH_glcm_Imc1 wavelet_LHH_gldm_SmallDependenceLowGrayLevelEmphasis wavelet_LHH_glszm_GrayLevelNonUniformity wavelet_LHH_glszm_ZoneEntropy
Recurrence model	9	exponential_gldm_DependenceNonUniformity exponential_gldm_DependenceVariance exponential_glrlm_ShortRunLowGrayLevelEmphasis lbp_3D_k_glrlm_ShortRunLowGrayLevelEmphasis lbp_3D_k_glszm_SmallAreaHighGrayLevelEmphasis wavelet_HLH_glcm_MaximumProbability wavelet_HLH_gldm_DependenceVariance wavelet_HLH_glszm_ZoneVariance wavelet_LLH_firstorder_Range

2D-SWE Two-dimensional shear wave elastography, *CCI* Comprehensive Complication Index

Table 4 Comparison of clinical signature, Rad signature, and the nomogram in CCI model and recurrence model

Signature		Accuracy	AUC	95% CI	Sensitivity	Specificity	PPV	NPV	Precision
CCI model	clinical signature-training	0.756	0.724	0.6538—0.7933	0.779	0.619	0.925	0.317	0.925
	Rad signature-training	0.626	0.862	0.8275—0.8973	0.563	1.000	1.000	0.279	1.000
	Nomogram -training	0.826	0.896	0.8613—0.9305	0.826	0.825	0.966	0.444	0.966
	clinical signature-validation	0.503	0.647	0.5799—0.7142	0.447	0.841	0.944	0.202	0.944
	Rad signature-validation	0.780	0.827	0.7722—0.8813	0.788	0.730	0.945	0.368	0.945
	Nomogram-validation	0.780	0.832	0.7777—0.8856	0.786	0.746	0.948	0.370	0.948
Recurrence model	clinical signature-training	0.614	0.574	0.5012—0.6468	0.627	0.543	0.880	0.215	0.880
	Rad signature-training	0.906	0.884	0.8326—0.9352	0.919	0.836	0.969	0.651	0.969
	Nomogram -training	0.803	0.854	0.8038—0.9047	0.813	0.746	0.946	0.420	0.946
	clinical signature-validation	0.508	0.552	0.4826—0.6209	0.477	0.671	0.886	0.194	0.886
	Rad signature-validation	0.642	0.839	0.8029—0.8741	0.577	1.000	1.000	0.300	1.000
	Nomogram-validation	0.663	0.844	0.8039—0.8840	0.604	0.985	0.996	0.311	0.996

CCI Comprehensive Complication Index, *Rad signature* Two-dimensional shear wave elastography radiomic signatures, *clinical signature* the combined signatures of laboratory, pathology, immunohistochemistry, etc.; *nomogram* the combined model of Rad signature and clinical signature, *AUC* Area Under Curve, *CI* confidence interval, *PPV* positive predictive value, *NPV* negative predictive value

employed singly, displayed enhanced prognostic value over its combination with other metrics. Such a discovery paves the way for a potential hypothesis: elastography-centric radiomics might play a pivotal role in predicting post-hepatectomy recurrence in HCC, albeit the necessity to include other imaging benchmarks for a comprehensive comparison. DCA also came into play, assessing each model's merit. Figures 5FG and 6FG,

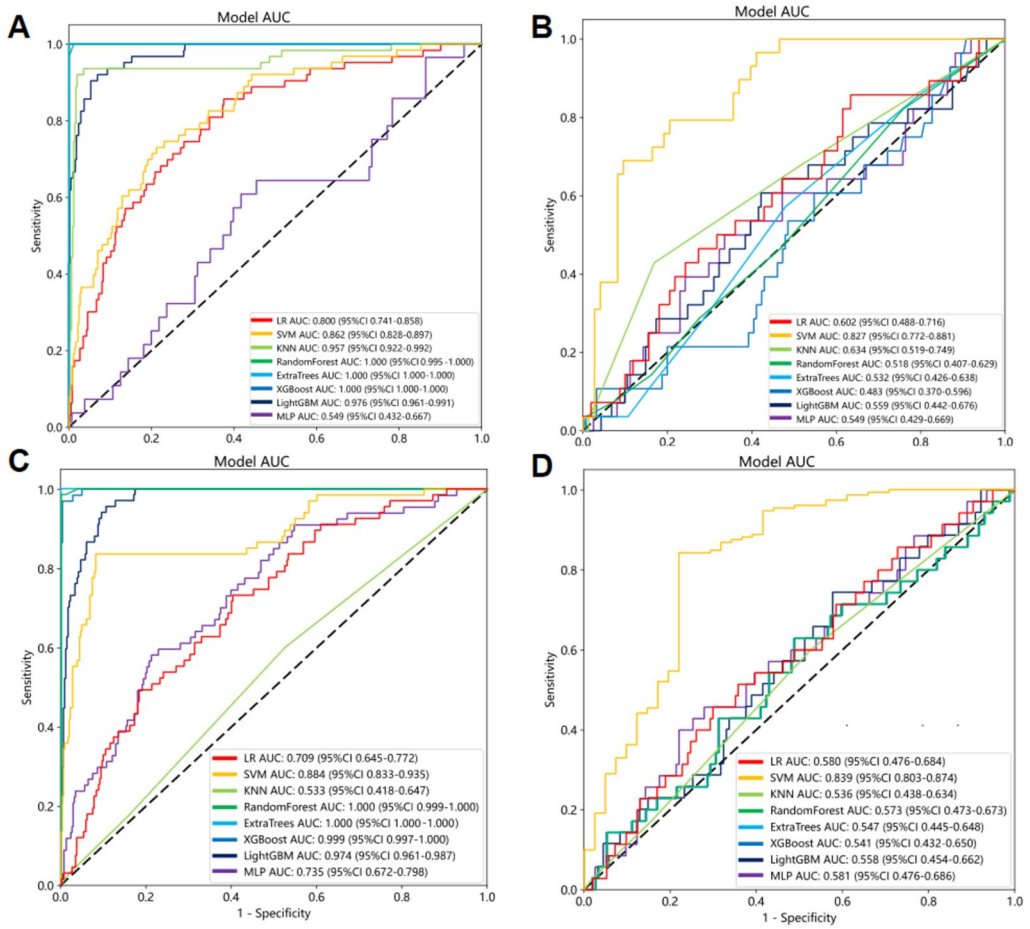

Fig. 4 Each Rad signature model's AUC on training and validation cohort in two models

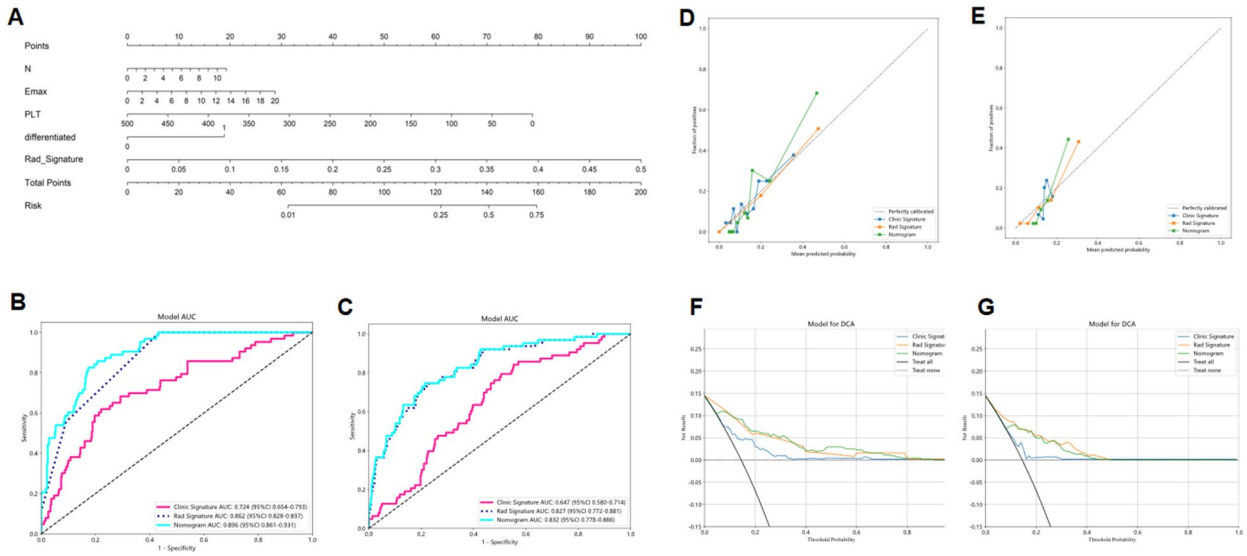

Fig. 5 Performance of the radiomics models

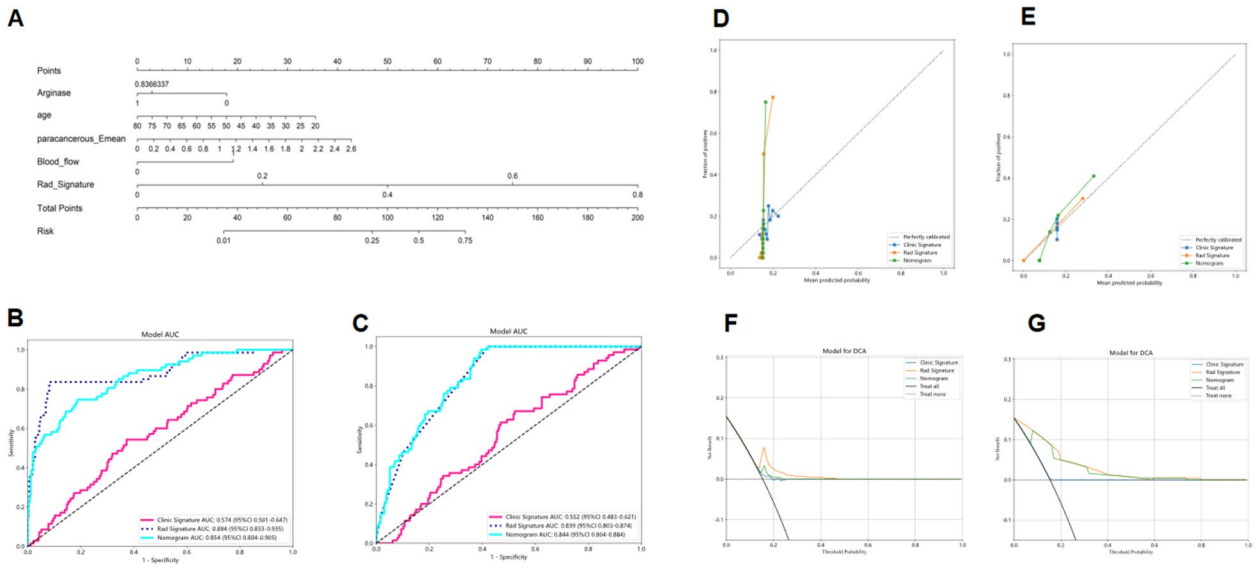

Fig. 6 Performance of radiomics models in relation to recurrence of HCC patients

respectively, present DCA for clinical, Rad signature, and the radiomic nomogram. The study further underscores the enhanced clinical relevance of 2D-SWE-centric radiomics in prognosticating high CCI and the likelihood of a recurrence within a year.

The data suggest a compelling notion that primary reliance for post-hepatectomy recurrence prediction in hepatocellular carcinoma might be on radiomics grounded in elastography. Yet, it remains imperative to factor in alternative imaging indicators for a holistic assessment. In this research, the utility of DCA was tapped to scrutinize each model. Figures 5FG and 6FG illustrate the decision curve analytical outcomes for the clinical, wheel signatures, and the radiomic nomogram. Notably, the prognostic capabilities of radiomics anchored in 2D-SWE in forecasting elevated CCI and a one-year recurrence have been underscored.

Table 5 The DELONG test was assessed clinical signature, Rad signature, and nomogram in CCI model and recurrence model

cohort	Nomogram vs. Clinical	Nomogram vs. Rad	Rad vs. Clinical
CCI-Training	< 0.001	0.002	< 0.001
CCI-validation	< 0.001	0.007	< 0.001
recurrence-Training	< 0.001	0.09	< 0.001
recurrence-validation	< 0.001	0.58	< 0.001

CCI Comprehensive Complication Index, *Rad signature* Two-dimensional shear wave elastography radiomic signatures, *clinical signature* the combined signatures of laboratory, pathology, immunohistochemistry, etc.; *nomogram* the combined model of Rad signature and clinical signature

Discussion

In treating HCC, hepatectomy has been established as a pivotal intervention, be it in early, moderate, or advanced stages [24–26]. Challenges post-hepatectomy encompass perioperative complications [27] and heightened recurrence risks. Recognizing those at an elevated risk becomes imperative to facilitate timely interventions. A salient revelation from the present research suggests that radiomics rooted in elastography, when incorporated as a pivotal determinant, can effectively stratify patients susceptible to elevated CCI and recurrence risks. Emphasizing the comprehensive nature of CCI, it offers insights into the intensity of surgical complications. A direct correlation exists between the severity of surgical complications in HCC patients and the propensity for postoperative recurrence. Elevated CCI scores often signify intensified surgical complications, due to impaired physiological recovery and weakened immune function, thereby amplifying recurrence risks postoperatively [28]. This research thus led to the formulation of distinct models for assessing CCI and recurrence, each exhibiting commendable prognostic capacities.

In exploring the prognosis of high CCI following hepatectomy, a conspicuous positive correlation was established between liver stiffness and elevated CCI [29]. Metrics embodying liver elasticity, notably Emax and Emean, serve as representational indicators in this study. Distinctly, within the training cohort, heightened values were evident in the recurrence group as opposed to its non-recurrence counterpart, harmonizing with prior scientific inquiries. Moreover, Emax emerged as an independent risk factor upon engaging multivariate

regression analysis. The Aspartate aminotransferase-platelet ratio index (APRI) and platelet albumin score (PAL) have previously been implicated in associations with augmented perioperative mortality and diminished overall survival rates among patients subjected to hepatectomy [30, 31]. Presently, APRI is incorporated as a mortality-associated predictive factor in the hepatectomy selection process. Notably, this study has spotlighted platelet count as an autonomous risk factor, wherein a reduction in platelet counts correlates with a surge in CCI. The neutrophil count, acknowledged as an independent risk factor, is conversely linked with an unfavorable prognosis, an association potentially arising from liver infiltration by neutrophils, which further nurtures an inflammatory microenvironment and triggers immune cell activation [32]. Ongoing research is notably steering toward neutrophil targeting as a prospective therapeutic strategy [33]. In relation to poorly differentiated liver cancer, a significant association with suboptimal prognosis has been identified, potentially attributable to characteristic deep infiltration into liver tissue and vascular invasion, factors often contribute to disease progression after surgery and facilitate metastasis in alternate organs [34].

Age delineates itself as a pivotal independent risk factor in forecasting relapse in postoperative contexts. Specifically, younger patients who undergo surgical intervention for liver cancer manifest a heightened susceptibility to recurrence, potentially attributable to the pronounced malignancy, expedited growth, and marked invasiveness of the tumor [35]. This susceptibility might be intertwined with aspects like genetic mutations and aberrations in the signaling pathways of patients. This research underscores that the positive expression of arginase, a critical enzyme in modulating amino acid metabolism, portends an unfavorable prognosis [36]. Antecedent studies have illuminated that arginase, through modulating amino acid metabolic processes, can instigate alterations therein, which, in turn, influence the energy metabolism and proliferative characteristics of tumor cells, fostering the recurrence of liver cancer in due course. An escalation in arginase levels might stifle immune functionality, thereby diminishing the immune cells' cytotoxic impacts on tumor entities [37], paving the way for liver cancer cells to circumvent immune detection and escalating the recurrence risk. The present study identifies elevated blood flow as an independent risk factor instrumental in precipitating early recurrence in HCC, potentially due to its role in delivering an abundance of nutrients and oxygen to the metabolically active and rapidly proliferating liver cancer cells, thereby fueling their growth and proliferative activities [38]. Historical research data underscore that liver cancer recurrence can instigate tumor angiogenesis, frequently correlated with enhanced invasiveness and metastatic capability [39].

2D-SWE radiomics melds the benefits of both 2D-SWE and radiomics, acting as an ultrasound-based image evaluation technique, which presently finds utility across varied facets of HCC. This method provides a conduit for diagnosing and distinguishing liver diseases by scrutinizing the elastic attributes of the lesion-involved tissue [40, 41]. Employing 2D-SWE radiomics for the quantitative gauging of elastic parameters enables the assessment of liver disease prognoses [42]. Furthermore, this technique can facilitate the observation of the hepatic cancer response throughout the treatment process [43]. Despite its capabilities, prior studies have predominantly leaned on hardness values, presenting a potential for operator-influenced subjectivity. The current research expands upon this by employing 2D-SWE radiomics for simultaneous prediction of complications and early recurrence episodes, yielding encouraging outcomes. Notably, the prognostic assessment efficacy of this methodology demonstrates substantial effectiveness.

In developing radiomics-based prediction models, we addressed the challenges of high-dimensional data, particularly overfitting and feature instability, by applying LASSO regression. The optimal penalty parameter (λ) was selected via tenfold cross-validation to balance model complexity and generalizability. To ensure feature reproducibility, only radiomic features with high inter-observer agreement (ICC > 0.80) were retained, minimizing variability from ROI segmentation. These stable features were used to build models for predicting CCI and early recurrence. Model performance was evaluated not only by AUC but also by DCA. These strategies—including LASSO regularization, cross-validation, feature stability filtering, and multi-metric evaluation—were employed to reduce bias and enhance the reliability and clinical applicability of our models.

Certain limitations within this study warrant attention and discussion. Initially, the findings elucidated herein originate from a dataset singularly derived from one center, thereby potentially circumscribing the results' applicability and generalizability to diverse populations and varied settings. Consequently, to affirm the robustness and application viability of the proffered models, external validation, facilitated by employing independent datasets sourced from several centers, becomes imperative. Additionally, the absence of data pertaining to long-term follow-up emerges as a subsequent limitation within the confines of this investigation. For a comprehensive evaluation of the recurrence model's predictive accuracy, securing and scrutinizing long-term outcome data remain paramount.

Conclusively, the establishment of two predictive models, intricately built upon 2D-SWE radiomics signatures, has been executed in this investigation. Each model demonstrates notable predictive performance and exhibits commendable predictive value concerning the manifestation of severe complications subsequent to hepatectomy, as well as in relation to short-term recurrences among HCC patients. Noteworthy is the substantial proficiency showcased by the application of 2D-SWE radiomics features in isolation, particularly in forecasting early recurrence with notable precision. This approach not merely facilitates the identification of individuals at elevated risk following hepatectomy, warranting early intervention, but also minimizes errors in subjective assessment inherently tied to ultrasound imaging techniques. Hence, this potential highlights the considerable potential for broader clinical adoption in broader contexts.

What is already known on this topic:

Prior to this study, predicting post-hepatectomy complications and early recurrence in hepatocellular carcinoma (HCC) patients remained challenging.
Existing methods lacked the precision and effectiveness needed for timely medical responses in managing these patients post-surgery.

What this study adds:

This study introduces and validates new predictive models based on radiomic features from two-dimensional shear wave elastography (2D-SWE) for forecasting complications and early recurrence in HCC patients after hepatectomy.
The Comprehensive Complication Index (CCI) and recurrence models demonstrated high predictive accuracy, with area under the receiver operating characteristic curve (AUC) values of 0.896 and 0.854, respectively.
Notably, the 2D-SWE radiomic signature showed superior predictive capacity for short-term recurrences compared to the recurrence model alone.

How this study might affect research, practice, or policy:

The findings from this study have significant implications for clinical practice in managing HCC patients.
The models could be instrumental in identifying patients at elevated risk for postoperative complications and recurrence, allowing for more tailored and timely medical interventions.
This approach may also guide future research in enhancing predictive methodologies and refining patient management strategies in HCC and other similar conditions.

Abbreviations

HCC	Hepatocellular carcinoma
CCI	Comprehensive Complication Index
2D-SWE	Two-dimensional shear wave elastography
AUC	Area under the receiver operating characteristic curve
CI	Confidence interval

Author contributions

Conception and design of the research: Dong Jiang, Jialun Ren, Yi Qian, and Yiran Li Acquisition of data: Dong Jiang, Jialun Ren, and Yi Qian Analysis and interpretation of data: Dong Jiang, Jialun Ren, Yi Qian, Yijun Gu, Ru Wang, Hua Yu, Hui Dong, Dongyu Chen, Yan Chen, and Haozheng Jiang Statistical analysis: Yijun Gu, Ru Wang, Hua Yu, Hui Dong, Dongyu Chen, Yan Chen, and Haozheng Jiang Drafting the manuscript: Dong Jiang, Jialun Ren, and Yi Qian Revision of manuscript for important intellectual content: Yiran Li.

Funding

This study was supported by the Eastern Hepatobiliary Surgery Hospital National Natural Science Foundation Youth Cultivation Project (2021GZR003) and Eastern Hepatobiliary Surgery Hospital Youth Cultivation Project in Medical and Engineering Interdisciplinary Research (2022YGJC001).

Data availability

No datasets were generated or analysed during the current study.

Declarations

Ethics approval and consent to participate

This study is supported by the Third Affiliated Hospital of the Second Military Medical University (Shanghai Oriental Hepatobiliary Surgery Hospital), Approval Number: EHBHKY2021-K-011.

Consent for publication

Not applicable.

Competing interests

The authors declare no competing interests.

Received: 4 November 2024 Accepted: 24 July 2025
Published online: 08 August 2025

References

1. Orci LA, Sanduzzi-Zamparelli M, Caballol B, Sapena V, Colucci N, Torres F, Bruix J, Reig M, Toso C. Incidence of hepatocellular carcinoma in patients with nonalcoholic fatty liver disease: a systematic review, meta-analysis, and meta-regression. Clin Gastroenterol Hepatol. 2022;20(2):283-292.e10.
2. McGlynn KA, Petrick JL, El-Serag HB. Epidemiology of hepatocellular carcinoma. Hepatology. 2021;73(1):4–13.
3. Søreide JA, Deshpande R. Post hepatectomy liver failure (PHLF)-Recent advances in prevention and clinical management. Eur J Surg Oncol. 2021;47(2):216–24.
4. Saadat LV, Goldman DA, Gonen M, Soares KC, Wei AC, Balachandran VP, Kingham TP, Drebin J, Jarnagin WR, D'Angelica MI. Timing of complication and failure to rescue after hepatectomy: single-institution analysis of 28 years of hepatic surgery. J Am Coll Surg. 2021;233(3):415–25.

5. Calthorpe L, Rashidian N, Cacciaguerra AB, Conroy PC, Hibi T, Hilal MA, Hoffman D, Park KM, Wang J, Adam MA, Alseidi A. International Post-Hepatectomy Liver Failure Study Group. Using the comprehensive complication index to rethink the ISGLS criteria for post-hepatectomy liver failure in an international cohort of major hepatectomies. Ann Surg. 2023;277(3):e592–6.
6. Xing H, Zhang WG, Cescon M, et al. Defining and predicting early recurrence after liver resection of hepatocellular carcinoma: a multi-institutional study. HPB (Oxford). 2020;22(5):677–89.
7. Chan AWH, Zhong J, Berhane S, et al. Development of pre and post-operative models to predict early recurrence of hepatocellular carcinoma after surgical resection. J Hepatol. 2018;69(6):1284–93.
8. Xing H, Sun LY, Yan WT, et al. Repeat hepatectomy for patients with early and late recurrence of hepatocellular carcinoma: a multicenter propensity score matching analysis. Surgery. 2021;169(4):911–20.
9. Yang Y, Lin K, Liu L, Qian Y, Yang Y, Yuan S, Zhu P, Huang J, Liu F, Gu F, FuS JB, Liu H, Pan Z, Lau WY, Zhou W. Impact of preoperative TACE on incidences of microvascular invasion and long-term post-hepatectomy survival in hepatocellular carcinoma patients: a propensity score matching analysis. Cancer Med. 2021;10(6):2100–11.
10. Raevens S, Boret M, Fallon MB. Hepatopulmonary syndrome. JHEP Rep. 2022;4(9): 100527.
11. Chan AWH, Zhong J, Berhane S, Toyoda H, Cucchetti A, Shi K, Tada T, ChongCCN XBD, Li LQ, Lai PBS, Mazzaferro V, García-Fiñana M, Kudo M, Kumada T, Roayaie S, Johnson PJ. Development of pre and post-operative models to predict early recurrence of hepatocellular carcinoma after surgical resection. J Hepatol. 2018;69(6):1284–93.
12. Mai RY, Wang YY, Bai T, Chen J, Xiang BD, Wu GB, Wu FX, Li LQ, Ye JZ. Combination Of ALBI And APRI To Predict Post-Hepatectomy Liver Failure AfterLiver Resection For HBV-Related HCC Patients. Cancer Manag Res. 2019;11:8799–806.
13. Lam CM, Fan ST, Yuen AW, Law WL, Poon K. Validation of POSSUM scoring systems for audit of major hepatectomy. Br J Surg. 2004;91(4):450–4.
14. Lee DH, Lee ES, Bae JS, Lee JY, Han JK, Yi NJ, Lee KW, Suh KS, Kim H, Lee KB, Choi BI. 2D shear wave elastography is better than transient elastography in predicting post-hepatectomy complication after resection. Eur Radiol. 2021;31(8):5802–11.
15. Marasco G, Colecchia A, Colli A, Ravaioli F, Casazza G, Bacchi Reggiani ML, Cucchetti A, Cescon M, Festi D. Role of liver and spleen stiffness in predicting the recurrence of hepatocellular carcinoma after resection. J Hepatol. 2019;70(3):440–8.
16. Li G, Li L, Li Y, Qian Z, Wu F, He Y, Jiang H, Li R, Wang D, Zhai Y, Wang Z, Jiang T, Zhang J, Zhang W. An MRI radiomics approach to predict survival and tumour-infiltrating macrophages in gliomas. Brain. 2022;145(3):1151–61.
17. Peng Z, Wang Y, Wang Y, Jiang S, Fan R, Zhang H, Jiang W. Application of radiomics and machine learning in head and neck cancers. Int J Biol Sci. 2021;17(2):475–86.
18. Slankamenac K, Nederlof N, Pessaux P, de Jonge J, Wijnhoven BP, Breitenstein S, Oberkofler CE, Graf R, Puhan MA, Clavien PA. The comprehensive complication index: a novel and more sensitive endpoint for assessing outcome and reducing sample size in randomized controlled trials. Ann Surg. 2014;260(5):757–62.
19. Tahiri M, Sikder T, Maimon G, Teasdale D, Hamadani F, Sourial N, Feldman LS, Guralnick J, Fraser SA, Demyttenaere S, Bergman S. The impact of postoperative complications on the recovery of elderly surgical patients. Surg Endosc. 2016;30(5):1762–70.
20. Gao Y, Guo F, Lu Z, Xi C, Wei J, Jiang K, Miao Y, Wu J, Chen J. Perioperative safety and prognosis following parenchyma-preserving surgery for solid pseudopapillary neoplasm of the pancreas. World J Surg Oncol. 2023;21(1):119.
21. Clavien PA, Barkun J, de Oliveira ML, Vauthey JN, Dindo D, Schulick RD, de Santibañes E, Pekolj J, Slankamenac K, Bassi C, Graf R, Vonlanthen R, Padbury R, Cameron JL, Makuuchi M. The Clavien-Dindo classification of surgical complications: five-year experience. Ann Surg. 2009;250(2):187–96.
22. Tian WS, Lin MX, Zhou LY, et al. Maximum value measured by 2-D shear wave elastography helps in differentiating malignancy from benign focal liver lesions. Ultrasound Med Biol. 2016;42(9):2156–66.
23. Park HS, Kim YJ, Yu MH, et al. Shear wave elastography of focal liver lesion: intraobserver reproducibility and elasticity characterization. Ultrasound Q. 2015;31(4):262–71.
24. Orcutt ST, Anaya DA. Liver resection and surgical strategies for management of primary liver cancer. Cancer Control. 2018;25(1):1073274817744621.
25. Liu D, Song T. Changes in and challenges regarding the surgical treatment of hepatocellular carcinoma in China. Biosci Trends. 2021;15(3):142–7.
26. Llovet JM, Kelley RK, Villanueva A, Singal AG, Pikarsky E, Roayaie S, Lencioni R, Koike K, Zucman-Rossi J, Finn RS. Hepatocellular carcinoma. Nat Rev Dis Primers. 2021;7(1):6.
27. Chen ZX, Schwartz M, Gu LH, Liang L, Wang P, Cescon M, Li JD, Liang YJ, PuJL ZYH, Wang H, Gu WM, Chen TH, Chen ZY, Wang MD, Li C, Zhang CW, Pawlik TM, Lau WY, Shen F, Liu FB, Yang T. Development and validation of safety and efficacy-associated risk calculator for hepatocellular carcinoma in the elderly after resection (SEARCHER): A multi-institutional observational study. Int J Surg. 2022;106:106842.
28. Yamashita S, Sheth RA, Niekamp AS, Aloia TA, Chun YS, Lee JE, Vauthey JN, Conrad C. Comprehensive complication index predicts cancer-specific survival after resection of colorectal metastases independent of RAS mutational status. Ann Surg. 2017;266(6):1045–54.
29. Serenari M, Han KH, Ravaioli F, Kim SU, Cucchetti A, Han DH, Odaldi F, Ravaioli M, Festi D, Pinna AD, Cescon M. A nomogram based on liver stiffness predicts postoperative complications in patients with hepatocellular carcinoma. J Hepatol. 2020;73(4):855–62.
30. Maegawa FB, Shehorn L, Aziz H, Kettelle J, Jie T, Riall TS. Association between noninvasive fibrosis markers and postoperative mortality after hepatectomy for hepatocellular carcinoma. JAMA Netw Open. 2019;2(1):e187142.
31. Meira Júnior JD, Fonseca GM, Carvalho Neto FN, Jeismann VB, Kruger JAP, Silva JPM, Coelho FF, Herman P. Platelet-albumin (PAL) score as a predictor of perioperative outcomes and survival in patients with hepatocellular carcinoma undergoing liver resection in a Western center. Surg Oncol. 2022;42: 101752.
32. Liu Y, Yan P, Bin Y, Qin X, Wu Z. Neutrophil extracellular traps and complications of liver transplantation. Front Immunol. 2022;17(13):1054753. https://doi.org/10.3389/fimmu.2022.1054753.
33. Geh D, Leslie J, Rumney R, Reeves HL, Bird TG, Mann DA. Neutrophils as potential therapeutic targets in hepatocellular carcinoma. Nat Rev Gastroenterol Hepatol. 2022;19(4):257–73.
34. Shen J, Liu J, Li C, Wen T, Yan L, Yang J. The impact of tumor differentiation on the prognosis of HBV-associated solitary hepatocellular carcinoma following hepatectomy: a propensity score matching analysis. Dig Dis Sci. 2018;63(7):1962–9.
35. Wang Q, Qiao W, Zhang H, Liu B, Li J, Zang C, Mei T, Zheng J, Zhang Y. Nomogram established on account of Lasso-Cox regression for predicting recurrence in patients with early-stage hepatocellular carcinoma. Front Immunol. 2022;13:1019638.
36. Grzywa TM, Sosnowska A, Matryba P, Rydzynska Z, Jasinski M, Nowis D, Golab J. Myeloid cell-derived arginase in cancer immune response. Front Immunol. 2020;11:938.
37. Tang Y, Xu L, Ren Y, Li Y, Yuan F, Cao M, Zhang Y, Deng M, Yao Z. Identification and validation of a prognostic model based on three mvi-related genes in hepatocellular carcinoma. Int J Biol Sci. 2022;18(1):261–75.
38. Ni Z, Wu B, Li M, Han X, Hao X, Zhang Y, Cheng W, Guo C. Prediction model and nomogram of early recurrence of hepatocellular carcinoma after radiofrequency ablation based on logistic regression analysis. Ultrasound Med Biol. 2022;48(9):1733–44.
39. Muraishi N, Kawamura Y, Akuta N, Shindoh J, Matsumura M, Okubo S, Fujiyama S, Hosaka T, Saitoh S, Sezaki H, Suzuki F, Suzuki Y, Ikeda K, Arase Y, Hashimoto M, Yasuda I, Kumada H. The impact of lenvatinib on tumor blood vessel shrinkage of hepatocellular carcinoma during treatment: an imaging-based analysis. Oncology. 2023;101(2):134–44.
40. Wang K, Lu X, Zhou H, Gao Y, Zheng J, Tong M, Wu C, Liu C, Huang L, Jiang T, Meng F, Lu Y, Ai H, Xie XY, Yin LP, Liang P, Tian J, Zheng R. Deep learning Radiomics of shear wave elastography significantly improved diagnostic performance for assessing liver fibrosis in chronic hepatitis B: a prospective multicentre study. Gut. 2019;68(4):729–41.
41. Wang W, Zhang JC, Tian WS, Chen LD, Zheng Q, Hu HT, Wu SS, Guo Y, Xie XY, Lu MD, Kuang M, Liu LZ, Ruan SM. Shear wave elastography-based ultrasomics: differentiating malignant from benign focal liver lesions. Abdom Radiol. 2021;46(1):237–48.

42. Jin J, Yao Z, Zhang T, Zeng J, Wu L, Wu M, Wang J, Wang Y, Yu J, Zheng R. Deep learning radiomics model accurately predicts hepatocellular carcinoma occurrence in chronic hepatitis B patients: a five-year follow-up. Am J Cancer Res. 2021;11(2):576–89.
43. Praktiknjo M, Krabbe V, Pohlmann A, Sampels M, Jansen C, Meyer C, Strassburg CP, Trebicka J, Gonzalez Carmona MA. Evolution of nodule stiffness might predict response to local ablative therapy: a series of patients with hepatocellular carcinoma. PLoS ONE. 2018;13(2): e0192897.

Publisher's Note

Springer Nature remains neutral with regard to jurisdictional claims in published maps and institutional affiliations.